Modeling Memoryless Degradation Under Variable Stress

Edward V. Thomas[1], Ira Bloom[2], Jon P. Christophersen[3], David C. Robertson[2], Lee K. Walker[2], Chinh D. Ho[3], and Vincent S. Battaglia[4]

[1]Sandia National Laboratories, Albuquerque, NM 87110-3436 USA
[2]Argonne National Laboratory, Argonne, IL 60439 USA
[3]Idaho National Laboratory, Idaho Falls, ID 83415 USA
[4]Lawrence Berkeley National Laboratory, Berkeley, CA 94720 USA

Abstract:

Accelerated degradation tests can be used as the basis for predicting the performance or state of health of products and materials at use conditions over time. Measurements acquired at accelerated levels of stress are used to develop models that relate to the degradation of one or more performance measures. Frequently, products/materials of interest are subjected to variable stress levels during their lifetimes. However, testing is usually performed only at a few fixed stress levels. In such cases, cumulative degradation models are developed and assessed by using data acquired under those fixed stress conditions. The degradation rate at any stress condition within the range of the model can be estimated by the derivative of the cumulative model at that stress condition. It follows that to predict cumulative degradation over variable use conditions, one might integrate the fluctuating degradation rate over time. Existing approaches for doing this consider degradation rates that depend only on the current stress level. Here, we propose to allow the degradation rate to also depend on the current state of health as indicated by the associated performance measure(s). The resulting modeling approach is capable of portraying a broader range of degradation behavior than existing approaches. The assertion of memoryless degradation by using this or any other approach should be assessed experimentally with data acquired under variable stress in order to increase confidence that the integrated rate model is accurate. In this paper, we demonstrate the additional capability of the proposed approach by developing empirical memoryless rate-based degradation models to predict resistance increase and capacity decrease in lithium-ion cells that are being evaluated for use in electric vehicles. We then assess the plausibility of these models.

Keywords: Accelerated Testing; Calendar Aging; Lithium-ion Batteries; Non-isothermal Stress; Parametric Bootstrap

Biographical Footnote

Dr. Thomas is a Statistician in Albuquerque, New Mexico. His email is edvthomas@msn.com.

Dr. Bloom is the Manager of the Electrochemical Analysis and Diagnostics Laboratory at Argonne National Laboratory. His email is Ira.bloom@anl.gov.

Dr. Christophersen is currently the Chief Scientist at Dynexus Technology. His email is jon.christophersen@dynexustech.com.

Mr. Robertson is an Engineering Specialist in the Chemical Science and Engineering Division at Argonne National Laboratory. His email is robertsond@anl.gov.

Mr. Walker is currently a Battery Research Engineering Specialist at Idaho National Laboratory. His email is lee.walker@inl.gov.

Mr. Ho is a Senior Research and Development Engineer for Idaho National Laboratory's Battery Test Center. His email is chinh.ho@inl.gov.

Dr. Battaglia is a Chemical Engineer at Lawrence Berkeley National Laboratory. His email is vsbattaglia@lbl.gov.

1. **Introduction**

Accelerated degradation tests are used to study changes in product performance over time at accelerated stress conditions (see e.g., Meeker and Escobar 1998 and Nelson 2004). Often, units are tested at one of several stress levels. In other cases, usually in the context of step-stress testing, units are tested at multiple stress levels (e.g., see Tseng and Wen 2000). Models based on the results of such testing are typically used to predict the degradation of the product at a target use condition. Accelerated degradation testing can provide significantly more information than other forms of accelerated tests, as useful information can be acquired from a test unit prior to its failure. Benefits include a better basis for accurate time extrapolation and an improved chance of finding a useful mechanistic model (e.g., see Meeker and Escobar 1993). Accelerated degradation tests involve one or more measures that relate to the state-of-health of a test unit. For example, the luminosity of a light emitting diode (LED) decreases as the LED ages (e.g., see Tseng and Wen 2000, Park and Bae 2010, and Cai et al. 2016). Failure occurs when the level of degradation increases beyond some critical limit. One objective is to model the progression of the degradation measure across stress conditions and time in order determine a product's useful life. The utility of a model is determined by its ability to accurately extrapolate performance from accelerated conditions to nominal use conditions. Models can be either empirical or physical/mechanistic (see e.g., Escobar and Meeker 2006). Common model forms relating to accelerated degradation data (and other forms of accelerated tests) are discussed in Escobar and Meeker 2006. Accelerated degradation testing has been used in association with a large variety of products such as integrated circuits (e.g., see Meeker, Escobar, and Lu 1998 and Santini et al. 2014), electrical meters (Yang et al. 2014), solar cells (Wang and Wong 2015) and rechargeable lithium-ion electrochemical cells which is the focus of our discussion here.

We discuss a simple experiment and associated analysis in which we examine the plausibility of memoryless degradation in the case of a particular design of lithium-ion cells that was being evaluated for use in electric vehicles. Knowledge concerning the degradation of lithium-ion cells is needed as the use of high-power and -energy lithium ion batteries in automotive applications, such as hybrid and plug-in hybrid electric and full-electric vehicles, is rapidly growing. Before these batteries can be used in such a demanding application, there must be some assurance that the life of the automotive battery is close to that of the vehicle, ~15 y. Batteries are deliberately oversized for use in new vehicles to allow for satisfactory performance following degradation

near a vehicle's end of life. Thus, battery life is often expressed in terms of the time that it takes for capacity and/or power to be degraded by some fixed relative amount (e.g., see Barré et al. 2013). In terms of capacity, the state of health of a battery is represented by the proportion of capacity remaining relative to its initial capacity. Loss of capacity reduces the range of electric vehicles. In addition, satisfactory acceleration of electrical vehicles requires a sufficient level of power from the battery. Power is adversely affected by increased cell resistance. The state of a battery might also be represented by its resistance relative to its initial state. Thus, the degradation measures that we focus on here are relative values of discharge capacity and cell resistance.

The life of a rechargeable battery is affected by both the conditions of its active use (charge/discharge cycling) and conditions during inactivity (calendar aging). In electric vehicle applications, batteries experience non-constant stress during periods of active use and periods of inactivity. The USABC (a consortium of Ford, Fiat-Chrysler Automobiles, General Motors and the US Department of Energy (DOE)) and the DOE have sponsored many efforts to accurately predict battery life to assure manufacturers and consumers that the long-life goal can be met (e.g., see Christophersen et al. 2006, Christophersen et al. 2007, Thomas et al. 2008, Gering et al. 2011, INL-EXT-08-15136 2012, and INL/EXT-14-32849 2014). These studies and others (e.g., see Wright et al. 2002, Bloom et al. 2003, Wohlfahrt-Mehrens et al. 2004, Broussely et al. 2005, Vetter et al. 2005, Zhang 2006, Anseán 2013, Barré et al. 2013, Han et al. 2014, Liu et al. 2016, and Xia et al. 2016) show that the estimation of battery life can be approached in a variety of ways and involve a variety of mechanisms. In this paper, we explore the effects of elevated temperature on calendar aging under non-isothermal conditions. Our main interest is to develop predictive models relating to the typical (average) degradation of cells under non-isothermal conditions. It is not our intent to predict reliability, per se, which can be greatly influenced by variation during production. Our focus is particularly relevant in early phases of product development where the goal is to establish whether or not a particular cell design has the basic capability to meet requirements.

With respect to calendar aging, the specific causes of capacity loss and resistance rise can vary depending on characteristics of the particular cell design including the associated anode, cathode, electrolyte, and binder materials (see e.g., Broussely et al. 2005, Vetter et al. 2005, Barré et al. 2013, and Han et al. 2014). It is generally accepted that the resistance rise is largely

due to thickening of a solid interface that protects the anode from possible corrosion and the electrolyte from reductions as well as decreases in accessible surface area over time. A major source of cell capacity loss is believed to be decomposition of the electrolyte which results in a loss of cyclable lithium. Nevertheless, the physical/chemical mechanisms associated with capacity loss and resistance rise vary across cell designs and are not understood with enough detail to allow for the development for quantitatively accurate mechanistic models of capacity loss and resistance rise. Note that this lack of detailed knowledge is expected to be more pronounced for cells in development as opposed to cells in high-volume production. Consequently, the goal here was to conduct a simple experiment to help empirically characterize the degradation behavior under non-isothermal stress for this particular cell design.

Using the nomenclature of Escobar and Meeker (2006), the experiment discussed here can be classified as an accelerated repeated measures degradation test (ARMDT). That is, nondestructive measurements of internal cell resistance and capacity were acquired at various points in time from a sample of cells being subjected to several regimes of high temperature stress which was used in order to accelerate the calendar aging process. A deterministic rate-based empirical model that is intrinsically memoryless is proposed to represent the expected paths of the degradation measures considered. Degradation models are formulated in terms of a non-decreasing relative response where the initial measurement of each cell is used as a basis to normalize subsequent measurements of that cell. Data acquired from cells subjected to isothermal and non-isothermal stress were used to estimate the parameters of degradation models relating to resistance increase and capacity loss. Uncertainty in the estimated model parameters is assessed via a parametric bootstrap procedure that is based on an observational model that incorporates cell-to-cell variation in the degradation rate as well as measurement error. The plausibility of the degradation models (and memoryless degradation) is assessed by using the ability of the models to predict average cell performance under both isothermal and non-isothermal conditions with consideration of uncertainties derived from the parametric bootstrap procedure.

The remainder of this paper describes the experiment, the various models and methods used to analyze the experimental data, and the fitted models. Section 2 describes the experiment including details of the stress conditions studied as well as the performance measurements that were acquired. Section 3 describes the forms of the deterministic and observational models as

well as the methods used to estimate model parameters and associated uncertainty. Section 4 presents fitted models for resistance increase and capacity loss and an assessment of the quality of the fits. Concluding remarks are given in Section 5.

2. **Experiment**

Commercially-available, high-power lithium-ion cells, which consisted of a Li(Mn, Co, Ni)O_2 + Li-Mn-O spinel cathode and a graphite anode were tested. They were 18650-sized cells (cylindrical cells about 18mm in diameter and 65mm in length) with a rated capacity of 1.2 Ah and a voltage range of 4.2 to 2.7 V. This size of cell is used in a variety of applications ranging from laptop computers to plug-in electric vehicles. Performance measurements were acquired via a Maccor series 4000 battery tester having a maximum voltage and current rating of 10 V and ±12.5 A, respectively. The test cells were placed in Tenney Junior temperature chambers that maintained ambient conditions of 45°C and 55°C during testing. We believe that testing at these accelerated conditions does not introduce new aging mechanisms unobserved under nominal conditions. We believe that the chamber temperatures were generally maintained very well within ±1°C of the targeted test profiles with a smaller level of variation in each chamber. The cells were stored at room temperature for about 2 months before testing starting.

Prior to being subjected to calendar life aging, all cells were characterized based on the plug-in hybrid electric vehicle requirements at 30°C in terms of C/1 capacity measurement (a rate at which the entire battery will discharge in an hour); a scaled, 10-kW, constant-power discharge; a low-current hybrid pulse power characterization test (HPPC) (see Battery Test Manual for Plug-In Hybrid Electric Vehicles 2014); an electrochemical impedance spectroscopy (EIS) measurement at 60% state of charge (SOC) (equivalent to open circuit voltage of 3.89 V) and C/25 charge and discharge capacity measurements. C/25 is a rate at which the entire battery will be charged or discharged in 25 hours. The reference performance test (RPT) consisted of the C/1 discharge capacity measurement, a scaled, 10-kW constant-power discharge, the HPPC test and the EIS measurement. The HPPC data were used to estimate cell resistance as a function of open circuit voltage. Cell resistance was estimated for each HPPC discharge and regen pulse (see Battery Test Manual for Plug-In Hybrid Electric Vehicles 2014). After characterization, RPT0 was performed at the start of testing and served as the basis from which performance decline was

determined. RPT's were conducted every 32 days at 30°C. The focus of the analysis here are the measurements of cell resistance and discharge capacity.

All cells were subjected to calendar life aging at 60% SOC. Cells were randomly assigned to treatment groups as shown in Table 1. The cells in Groups A and B were the isothermal control group, establishing baseline performance decay rates. The cells in Group C experienced only one temperature change, which occurred after three months during which an approximate 15% power fade was observed. The temperature for cells in Group D changed after each RPT.

TABLE 1. Distribution of Cells Versus Treatment Group

Group	Temperature(s), °C	Cell count
A	45	3
B	55	3
C	55-45	3
D	55-45-55-45-…	3

Calendar-life testing consisted of resting the cells at an open circuit voltage condition at the test temperature shown in Table 1. The cells were soaked at the target test temperature for at least 4 hours prior to the start of each calendar-life aging period to ensure thermal equilibrium. A pulse-per-day was also performed on the cells (see Battery Test Manual for Plug-In Hybrid Electric Vehicles 2014). The cells were placed in an open-circuit condition between each pulse during calendar aging. Every 32 days, the cells were cooled to 30°C and allowed to equilibrate for at least 4 hours before the RPT was performed. In all, 13 RPT's (RPT0, RPT1, …, RPT12) were performed over the course of slightly more than a year.

3. **Modeling Approach**

It is common to use elevated temperature to accelerate the calendar aging process. For the sake of simplicity, most battery tests are performed under isothermal conditions. Isothermal conditions facilitate a basic understanding of the underlying mechanisms which are responsible for the observed performance decline and capture the expected range of aging. However, a basic qualitative understanding of the underlying degradation mechanisms does not usually result in high fidelity, science-based, predictive models for resistance increase or capacity loss. Thus, we

are motivated to use controlled experiments to develop predictive statistical models that are empirical in nature. The usual intent is that models based on these results will accurately reflect the cumulative effects of exposure to a specific temperature. However, automotive applications do not generally involve static temperature conditions. Therefore, a cumulative degradation model defined in terms of a static temperature may not be useful to predict degradation of cells in these applications. Rather, we focus on modelling the instantaneous degradation rate as it underlies any assessment of cumulative degradation in a variable stress (i.e. non-isothermal) environment. We assume that the degradation measure contains useful information about the state of a cell. While the degradation rate might be expressed by differentiating the cumulative degradation models, a more straightforward approach is to consider a degradation rate model directly (e.g., see Chan and Meeker 2001 and Thomas et al. 2012). Once developed, the rate model can be integrated over the stress history to express the level of cumulative degradation.

Here, we develop degradation rate models that are formulated in terms of a non-decreasing relative response (e.g., see Thomas et al. 2008, 2012) that pertain directly to definitions of battery life. In the case of resistance, we consider relative resistance where the data used for modeling are the values of resistance from RPT1-12 divided by the corresponding cell-specific resistance values measured at RPT0. In the case of discharge capacity, we consider inverse relative capacity. Note that both measures of degradation (relative resistance and inverse relative capacity) mitigate the effects of cell-to-cell variation in the initial resistance and capacity measurements and have an initial value of one at RPT0. This normalization is important since cell-to-cell effects can be significant during pre-production phases of manufacturing. As the cells age, the expected values of both degradation measures increase.

The family of degradation rate models that we consider are memoryless, which means that the rate of degradation depends only on the current degradation state (measured by relative resistance or capacity) and the current stress level (temperature). Others (e.g., see Tseng and Wen 2000, Chan and Meeker 2001, and Peng and Tseng 2010) consider simplified forms of memoryless models where the rate of degradation depends only on the current stress level. We propose a broader class of rate models that also depend on the current state and therefore have the ability to portray a wider range of degradation behavior.

In order to assess the plausibility of the deterministic degradation models we also need a reasonable understanding of the levels of uncertainty in the estimated model parameters. We do this via a parametric bootstrap procedure that incorporates measurement error and cell-to-cell variation as sources of model uncertainty. These random effects are added to the deterministic model in order to form observational models that are derived specifically for each of the relative degradation measures used. The observational models are intended to provide an accurate description of the observed cell performance at use conditions over time and include the variances of the measurement error and cell-to-cell effects as additional parameters. The subsections that follow discuss the deterministic and observational models separately.

3.1 **Rate-Based Deterministic Degradation Model**

Here, either relative resistance or inverse relative capacity is used to indicate the state of the degradation process in a rate-based deterministic model framework, as described in Thomas et al. 2012. The underlying rate-based model has the form

$$\frac{dm(T[0,\tau])}{d\tau} = k(T(\tau)) \cdot m(T[0,\tau])^{\rho}, \quad (1)$$

where $m(T[0,\tau])$ is the theorized/expected value of either one of the relative degradation measures following exposure to a temperature profile given by $T[0,\tau]$, and *k* is a function of the instantaneous temperature at time τ, $T(\tau)$.

Equation (1) depicts one possible form of a memoryless process since the current degradation rate depends only on the assumed current state of the process, $m(T[0,\tau])$, and the current temperature, $T(\tau)$. Equation (1) could be generalized in many ways. For example, the degradation rate could be redefined to depend on multiple stress factors and measures of state. The rate of increase of both degradation measures considered is affected by *k*, which is assumed to be a non-decreasing function of temperature. In general, one might express *k* in terms of an Arrhenius or some other well-established model (e.g., see Escobar and Meeker 2006). Here, given the motive of this analysis, the limited temperature range, and number of temperature levels involved (two), we express $k\big(T(\tau)\big)$ as a simple linear function, $k\big(T(\tau)\big) = a + b \cdot T(\tau)$. While it is not possible to validate the linear rate dependence without data from additional temperature levels, the linear rate form will suffice here given that we need to evaluate $k\big(T(\tau)\big)$

at only two levels of temperature. The purpose of ρ is to provide additional modelling flexibility. If ρ is found to be indistinguishable from zero, this implies that the degradation rate remains constant over time for a given temperature. If ρ is found to be distinguishable from zero, this implies that the rate expressed in Equation (1) either increases ($\rho > 0$) or decreases ($\rho < 0$) over time for a given temperature. For example, a decreasing degradation rate might be caused by a loss of reactants due to consumption during previous degradation episodes.

The integration of Equation (1) over the temperature profile, $T[0,t]$, in combination with the initial condition ($m_{t=0} = 1$) yields an integral equation that provides the expected value of the degradation measure at time *t*,

$$m(T[0,t]) = 1 + \int_0^t k\big(T(\tau)\big) \cdot m(T[0,\tau])^{\rho} d\tau. \tag{2}$$

As indicated in Equation (2), the degradation measures depend on the aging temperature profile via $k\big(T(\tau)\big)$. Section 3.3 will discuss methods for estimating the model parameters (*a*, *b*, and ρ).

3.2 **Observational Models**

Due to measurement error and cell-to-cell variation, the observed values of the degradation measures for the j[th] cell, $M\big(T_j[0,t]\big)$, deviate from their expected values, $m\big(T_j[0,t]\big)$, where $T_j[0,t]$ represents the specific temperature profile experienced by the j[th] cell. In order to simplify the notation going forward, $M\big(T_j[0,t]\big)$ and $m\big(T_j[0,t]\big)$ will be referred to as $M_j(t)$ and $m_j(t)$, respectively. In the case of the resistance, we represent the observed degradation measure by

$$M_j(t) = \frac{Y_j(t)}{Y_j(0)} = \frac{y_j(t) + \varepsilon_j(t)}{y_j(0) + \varepsilon_j(0)}, \tag{3}$$

where $Y_j(t)$ is the measured resistance of the j[th] cell at time *t*, $y_j(t)$ is the true (unobserved) resistance, and $\varepsilon_j(t)$ is a random measurement error of resistance. The measurement errors are assumed to be independent with mean zero and variance σ_ε^2. Furthermore, it is assumed that

$$y_j(t) = y_j(0) \cdot \Big(m_j(t) + \delta_j \cdot \big(m_j(t) - 1\big)\Big), \tag{4}$$

where $y_j(0)$ and δ_j are cell-specific effects that could be regarded as natural consequences of manufacturing variation. Underlying cell-to-cell variation in the initial resistance (distinct from measurement error) is represented in Equation (4) by $y_j(0)$. In addition, δ_j is a random effect with mean zero and variance σ_δ^2 that represents cell-to-cell variation in rate of degradation. While Equation (4) is empirical, it reflects observed attributes of the degradation data that are considered here (see Section 4.1). It follows that

$$M_j(t) = \frac{y_j(0) \cdot \Big(m_j(t) + \delta_j \cdot \big(m_j(t) - 1\big)\Big) + \varepsilon_j(t)}{y_j(0) + \varepsilon_j(0)}. \tag{5}$$

Without loss of generality we simplify Equation (5) by letting $y_j(0) = 1$ and acknowledge that $\varepsilon_j(0)$ and $\varepsilon_j(t)$ must be correspondingly scaled. This results in

$$M_j(t) = \frac{m_j(t) + \delta_j \cdot \big(m_j(t) - 1\big) \ + \varepsilon_j(t)}{1 + \varepsilon_j(0)}. \tag{6}$$

In the case of the capacity, we represent the observed degradation measure by

$$M_j(t) = \frac{Y_j(0)}{Y_j(t)} = \frac{y_j(0) + \varepsilon_j(0)}{y_j(t) + \varepsilon_j(t)}, \tag{7}$$

where $Y_j(t)$ is the measured capacity, $y_j(t)$ is the true (unobserved) capacity, and $\varepsilon_j(t)$ is a random measurement error of capacity. In the case of capacity, we propose that

$$y_j(t) = y_j(0) \cdot \Big(1/\Big(m_j(t) + \delta_j \cdot \big(m_j(t) - 1\big)\Big)\Big). \tag{8}$$

With that assumption, it follows that

$$M_j(t) = \frac{y_j(0) + \varepsilon_j(0)}{y_j(0) \cdot \Big(1/\Big(m_j(t) + \delta_j \cdot \big(m_j(t) - 1\big)\Big)\Big) + \varepsilon_j(t)}. \tag{9}$$

Again, by letting $y_j(0) = 1$, Equation (9) can be represented as

$$M_j(t) = \frac{1 + \varepsilon_j(0)}{1/\Big(m_j(t) + \delta_j \cdot \big(m_j(t) - 1\big)\Big) + \varepsilon_j(t)}. \tag{10}$$

For purposes of fitting and assessing the fit of the degradation models, it is important to understand the uncertainty in the observed degradation measures. First, we assume that the random effects, δ_j and $\varepsilon_j(t)$, are sufficiently small relative to the true (unobserved measures). Given the magnitude of the random effects studied here, the expected value of $M_j(t)$ is essentially equal to $m_j(t)$. In other cases, a second-order Taylor-series expansion of $M_j(t)$ may be required in order to obtain a satisfactory approximation for the expectation of $M_j(t)$. First-order Taylor-series expansions of $M_j(t)$ are used to obtain the following approximation for the variance of $M_j(t)$.

$$Var\left(M_j(t)\right) \approx \left(\frac{\partial M_j(t)}{\partial \varepsilon_j(t)}\right)^2 \cdot Var\left(\varepsilon_j(t)\right) + \left(\frac{\partial M_j(t)}{\partial \varepsilon_j(0)}\right)^2 \cdot Var\left(\varepsilon_j(0)\right) + \left(\frac{\partial M_j(t)}{\partial \delta_j}\right)^2 \cdot Var(\delta_j), \quad (11)$$

where the partial derivates are evaluated at the expected values of $\varepsilon_j(0)$, $\varepsilon_j(t)$, and δ_j which are zero. In the case of relative resistance,

$$Var\left(M_j(t)\right) \approx \left(1 + m_j(t)^2\right) \cdot \sigma_\varepsilon^2 + \left(m_j(t) - 1\right)^2 \cdot \sigma_\delta^2. \quad (12)$$

In the case of inverse relative capacity,

$$Var\left(M_j(t)\right) \approx \left(m_j(t)^2 + m_j(t)^4\right)\sigma_\varepsilon^2 + \left(m_j(t) - 1\right)^2 \cdot \sigma_\delta^2. \quad (13)$$

We likewise obtain approximations for $Cov\left(M_j(t),\ M_j(t');\ t' \neq t\ \right)$. In the case of relative resistance, $Cov\left(M_j(t),\ M_j(t')\ ;\ t' \neq t\right) \approx$

$$\left[\frac{\sigma_\varepsilon^2}{\left(1+\sigma_\varepsilon^2\right)^2} + 1\right] \cdot \left\{m_j(t) \cdot m_j(t') + \sigma_\delta^2 \cdot \left(m_j(t) - 1\right) \cdot \left(m_j(t') - 1\right)\right\} - m_j(t) \cdot m_j(t')\ . \quad (14)$$

In the case of inverse relative capacity,

$Cov\left(M_j(t),\ M_j(t')\ ;\ t' \neq t\right) \approx$

$$[1 + \sigma_\varepsilon^2] \cdot \left\{m_j(t) \cdot m_j(t') + \sigma_\delta^2 \cdot \left(m_j(t) - 1\right) \cdot \left(m_j(t') - 1\right)\right\} - m_j(t) \cdot m_j(t')\ . \quad (15)$$

If the random effects are sufficiently small, these approximations are very accurate (see Section 4.1.1). By further assuming a distributional form for these effects, one can effectively use these approximations for estimating the complete set of model parameters (a, b, ρ, σ_ε^2, and σ_δ^2) by

using maximum likelihood methodology (see Section 3.3). Here, we will assume that the random effects are normally distributed.

3.3 **Methods to Estimate Model Parameters**

A three-step procedure was used to estimate the model parameters for each of the two responses. The first step was to obtain preliminary estimates of the parameters associated with the expected degradation rate (a, b, and ρ). This was accomplished via robust nonlinear least-squares regression using iteratively reweighted least squares implemented with a biweight weighting function (e.g., see Holland and Welsch 1977) with the tuning parameter, c, set to 4.685. At each iteration of the nonlinear regression procedure, predicted values of the given response were computed for each observation by using a numerical approximation to the integral in Equation (2) in association with the current, but evolving, parameter estimates. At each iteration, numerical predictions of $m_j(t)$, denoted by $\hat{m}_j(t)$ were obtained by subdividing t into one-hour intervals (Δt) using the simple method shown in Thomas et al. (2012) and summarized below in Table 2. In other cases where the stress level was changing rapidly, one could perhaps use smaller intervals and/or more precise forms of numerical integration.

TABLE 2. Numerical Prediction of Degradation Measure

Time, τ	$T(\tau)$	$\hat{m}_j(\tau)$
0	$T(0)$	$\hat{m}_j(0)=1$
Δt	$T(\Delta t)$	$\hat{m}_j(0) + \hat{k}\big(T(0)\big) \cdot \hat{m}_j(0)^{\hat{\rho}} \cdot \Delta t$
$2 \cdot \Delta t$	$T(2 \cdot \Delta t)$	$\hat{m}_j(\Delta t) + \hat{k}\big(T(\Delta t)\big) \cdot \hat{m}_j(\Delta t)^{\hat{\rho}} \cdot \Delta t$
⋮	⋮	⋮
$t = N \cdot \Delta t$	$T(t)$	$\hat{m}_j((N-1) \cdot \Delta t) + \hat{k}\big(T((N-1) \cdot \Delta t)\big) \cdot \hat{m}_j((N-1) \cdot \Delta t)^{\hat{\rho}} \cdot \Delta t$

The second step was to obtain preliminary estimates of the parameters associated with the random effects (σ_ε^2 and σ_δ^2) for each of the two responses. In the absence of results from a relevant measurement capability study, an initial estimate of the measurement error variance (σ_ε^2)

involves the predicted value of $m_j(t)$ and the observed sample variance of $M_j(t)$ for cells in Groups B, C, and D during RPT1, denoted by $\hat{m}_{BCD-1}$ and $\hat{V}ar(M_{BCD-1})$, respectively. These estimates of the measurement error variance are based on simplified versions of Equations (12) and (13). In the case of relative resistance,

$$\hat{\sigma}_{\varepsilon}^2(init) = \hat{V}ar(M_{BCD-1})/(1 + \hat{m}_{BCD-1}^2). \tag{16}$$

In the case of inverse relative capacity,

$$\hat{\sigma}_{\varepsilon}^2(init) = \hat{V}ar(M_{BCD-1})/(\hat{m}_{BCD-1}^2 + \hat{m}_{BCD-1}^4). \tag{17}$$

The rationale for using $\hat{V}ar(M_{BCD-1})$ and $\hat{m}_{BCD-1}^2$ is that all cells in Groups B, C, and D nominally received the same treatment through RPT1. Furthermore, the nature of the relative measures tends to mitigate the effects of cell-to-cell variation in the initial resistance and capacity measurements. The rationale for ignoring the contribution of $\left(m_j(t) - 1\right)^2 \cdot \sigma_{\delta}^2$ to $Var\left(M_j(t)\right)$ that is given in Equations (12) and (13) is that at RPT1, $\hat{m}_{BCD-1}^2$ is very nearly one and the computational contribution of $(\hat{m}_{BCD-1}^2 - 1)^2$ is minor unless σ_{δ}^2 is very large.

With an initial estimate for σ_{ε}^2 in hand, an initial estimate of the variance of the cell-specific effect is based on Equations (12) and (13). In the case of relative resistance,

$$\hat{\sigma}_{\delta}^2(init) = \underset{\hat{m}_{ir} \geq 1.2}{Mean} \left\{ \frac{\hat{V}ar(M_{ir}) - (1 + \hat{m}_{ir}^2) \cdot \hat{\sigma}_{\varepsilon}^2(init)}{(\hat{m}_{ir} - 1)^2} \right\}, \tag{18}$$

where M_{ir} represents the collective set of observed values of $M_j(t)$ associated with the ith treatment group and the rth RPT, $\hat{m}_{ir}$, represents the predicted value of $m_j(t)$, and $\hat{V}ar(M_{ir})$ represents the sample variance for that same set. In the case of inverse relative capacity,

$$\hat{\sigma}_{\delta}^2(init) = \underset{\hat{m}_{ir} \geq 1.2}{Mean\ (50\%)} \left\{ \frac{\hat{V}ar(M_{ir}) - (\hat{m}_{ir}^2 + \hat{m}_{ir}^4) \cdot \hat{\sigma}_{\varepsilon}^2(init)}{(\hat{m}_{ir} - 1)^2} \right\}, \tag{19}$$

Only those conditions where $\hat{m}_{ir} \geq 1.2$ are considered since the level of cell-to-cell divergence within a treatment group caused by δ_j is inconsequential and therefore largely uninformative at early stages of degradation.

The final step is to re-estimate the model parameters jointly by using maximum likelihood (M.L.) estimation. Let $\boldsymbol{d_j} = \{d_{jr} = M_j(r) - m_j(r), r = 1{:}\, n_r\}$, where d_{jr} represents the difference between observed and expected performance measures for the j[th] cell at the r[th] RPT. Given the previous assumptions concerning $\varepsilon_j(t)$ and δ_j, it follows that $\boldsymbol{d_j}$ and $\boldsymbol{d_{j'}}$ ($j' \neq j$) are independent. Given that $\varepsilon_j(t)$ and δ_j are assumed to be normally distributed, then $\boldsymbol{d_j}$ is approximately multivariate normal with zero mean and covariance, $\boldsymbol{\Sigma}_j$ (see Section 4.1.1). Equations 12-15 provide approximations for the diagonal and off-diagonal elements of $\boldsymbol{\Sigma}_j$ in terms of the model parameters. These equations involve σ_ε^2, σ_δ^2, and $m_j(r)$, which is defined by *a*, *b*, and ρ. With respect to the combined measurements of the j[th] cell, the likelihood function of $\boldsymbol{\theta} = \left(a, b, \rho, \sigma_\varepsilon^2, \sigma_\delta^2\right)$ is $L_j(\boldsymbol{\theta}) = f\left(\boldsymbol{d_j}; \mathbf{0}, \boldsymbol{\Sigma}_j(\boldsymbol{\theta})\right)$, where *f* is the multivariate normal pdf with mean zero and covariance $\boldsymbol{\Sigma}_j(\boldsymbol{\theta})$. Across measurements of all cells, the aggregate likelihood function of $\boldsymbol{\theta}$ is $L(\boldsymbol{\theta}) = \prod_{j=1}^{12} L_j(\boldsymbol{\theta}) = \prod_{j=1}^{12} f\left(\boldsymbol{d_j}; \mathbf{0}, \boldsymbol{\Sigma}_j(\boldsymbol{\theta})\right)$. The M.L. estimate of $\boldsymbol{\theta}$ is $\widehat{\boldsymbol{\theta}} = \left(\hat{a}, \hat{b}, \hat{\rho}, \hat{\sigma}_\varepsilon^2, \hat{\sigma}_\delta^2\right) = \boldsymbol{arg}\,\underset{\boldsymbol{\theta}}{\boldsymbol{max}}\, \hat{l}(\boldsymbol{\theta})$, where $\hat{l}(\boldsymbol{\theta}) = \sum_{j=1}^{12} ln\left(f\left(\widehat{\boldsymbol{d}}_j; \mathbf{0}, \widehat{\boldsymbol{\Sigma}}_j(\boldsymbol{\theta})\right)\right)$ and where $\widehat{\boldsymbol{d}}_j = \{\hat{d}_{jr} = M_j(r) - \hat{m}_j(r), r = 1{:}\, n_r\}$, $\widehat{\boldsymbol{\Sigma}}_j(\boldsymbol{\theta})$, and $\hat{m}_j(r)$ (which is a component of $\widehat{\boldsymbol{d}}_j$ and $\widehat{\boldsymbol{\Sigma}}_j(\boldsymbol{\theta})$) are based on estimates of the model parameters. Here, we rely on numerical optimization using the simplex search method as implemented in MATLAB (e.g., see Lagarias et al. 1998) by minimizing $-\hat{l}(\boldsymbol{\theta})$ with the function, *fminsearch*, to obtain $\widehat{\boldsymbol{\theta}}$. Initial estimates for *a*, *b*, and ρ were obtained by robust nonlinear regression. As discussed earlier, initial estimates for σ_ε^2 and σ_δ^2 were obtained via Equations 16-19.

As a caveat, note that while the estimates of σ_ε^2 and σ_δ^2 are intended to represent the levels of measurement error and cell-to-cell variation in the degradation rate, they are in fact non-specific. For example, systematic differences in temperature exposure within a treatment group (due to temperature variation within a temperature chamber) could inflate the estimate of cell-to-cell variation in the degradation rate. Furthermore, imperfect temperature control is a source of lack of fit associated with the degradation model. Finally, lack of fit with respect to the degradation model can affect the estimates of σ_ε^2 and σ_δ^2.

3.4 **Bootstrap Simulation**

The standard errors of the fitted degradation model parameters and other statistics were obtained by using a parametric bootstrap method (see e.g., Efron and Tibshirani 1993, Meeker, Escobar, and Lu 1998, and Thomas et al. 2008) involving 1000 simulation trials. Each simulation trial of the bootstrap procedure was designed to mimic the actual experiment in terms of test duration, RPT frequency, experimental conditions, and number of cells per condition. Random realizations of Gaussian distributed measurement errors, $\varepsilon_j(t)$, and cell-specific effects, δ_j, with zero mean and variances $\hat{\sigma}_\varepsilon^2$ and $\hat{\sigma}_\delta^2$, respectively, were added via Equation (6) (or Equation (10)) to the assumed truth as given by the fitted degradation models. Model parameters were estimated for each simulation trial. The bootstrap standard errors are derived from the ensemble of parameter estimates obtained from the simulation trials.

4. **Experimental Results and Fitted Models**

All of the data (Groups A, B, C, and D) were used to develop separate degradation models for relative resistance and inverse relative capacity. The models were used to predict the expected degradation paths for each temperature profile given in Table 1. The initial capacity and resistance measurements acquired at RPT0 are given in Table 3 for each of the treatment groups.

TABLE 3. Initial capacity and resistance values

Group	Capacity, Ah	Cell resistance at 60% SOC, mΩ
A	1.263, 1.264, 1.267	47.16, 47.83, 49.15
B	1.261, 1.265, 1.270	48.37, 48.37, 49.48
C	1.262, 1.262, 1.263	47.79, 47.86, 48.26
D	1.261, 1.263, 1.263	47.25, 47.58, 47.66

Figure 1 displays relative resistance versus inverse relative capacity for all cell measurements. The measurements are distinguished by treatment group. While relative resistance and inverse relative capacity are different metrics and may involve a mix of similar and different degradation mechanisms, it is interesting to observe that they are nearly equivalent everywhere except at the

highest degradation levels where relative resistance tends to exceed inverse relative capacity. This deviation between relative resistance and relative capacity occurs when the relative resistance exceeds 1.6 (e.g., see Group B cells at long exposure).

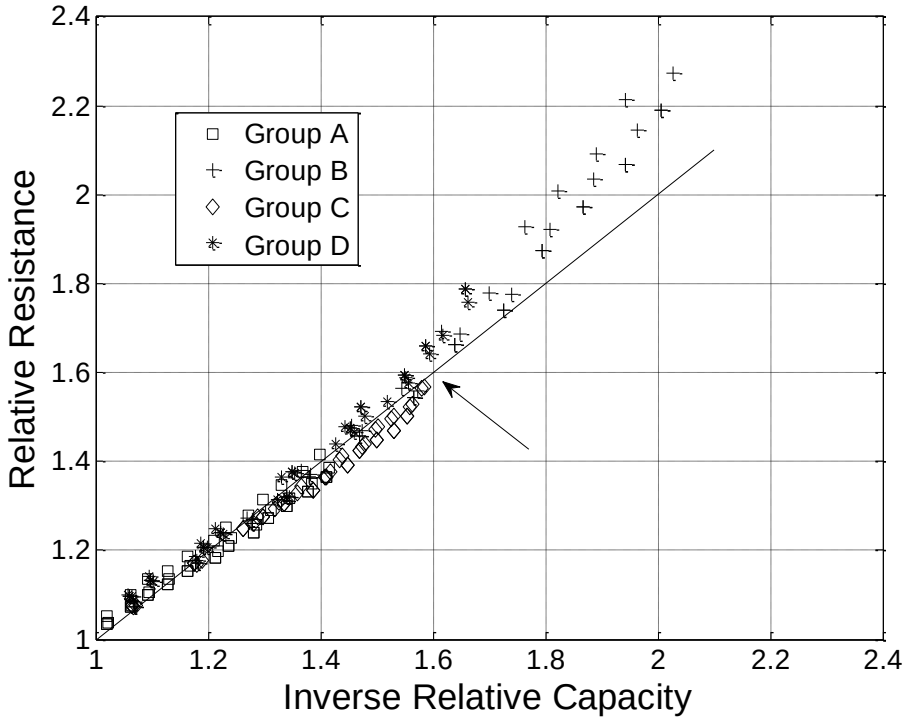

FIGURE 1. Relative resistance versus inverse relative capacity, by group. The arrow indicates where relative resistance and relative capacity begin to diverge.

4.1 **Resistance**

Figure 2 illustrates how the fitted relative resistance model obtained by M.L. estimation relates to the experimental data (by group) for all profiles. The initial and M.L. estimates of the degradation model parameters (a, b, and ρ) and variance components (σ_ε^2 and σ_δ^2) are given in Table 4. Note that $\hat{\rho}$ can be statistically distinguished from (and is larger than) zero. Consistent with $\rho > 0$, a close examination of the Group B data shows that the rate of increase in resistance appears to increase subtly as the resistance increases. Given that the average initial resistance was about 48 mΩ, it follows that the standard deviation of measurement error is estimated to be about 0.5 mΩ. An examination of the behavior of cells within treatment groups in Figure 2

reveals a divergence in performance over time. The nature of divergence is inconsistent with a Brownian motion process such as modeled by Peng and Tseng 2010, since the degradation paths observed generally continue to separate without crossover. However, the nature of divergence is consistent with unit-to-unit variability in the degradation rate, hence motivating the random effect, δ_j. Note that random unit-to-unit variability in the degradation rate (relating to the power of integrated circuits) was also observed and modeled by Meeker, Escobar, and Lu 1998. Based on the estimate of σ_δ^2, we conclude that the rate of relative resistance rise across cells varies with a standard deviation of about 5%.

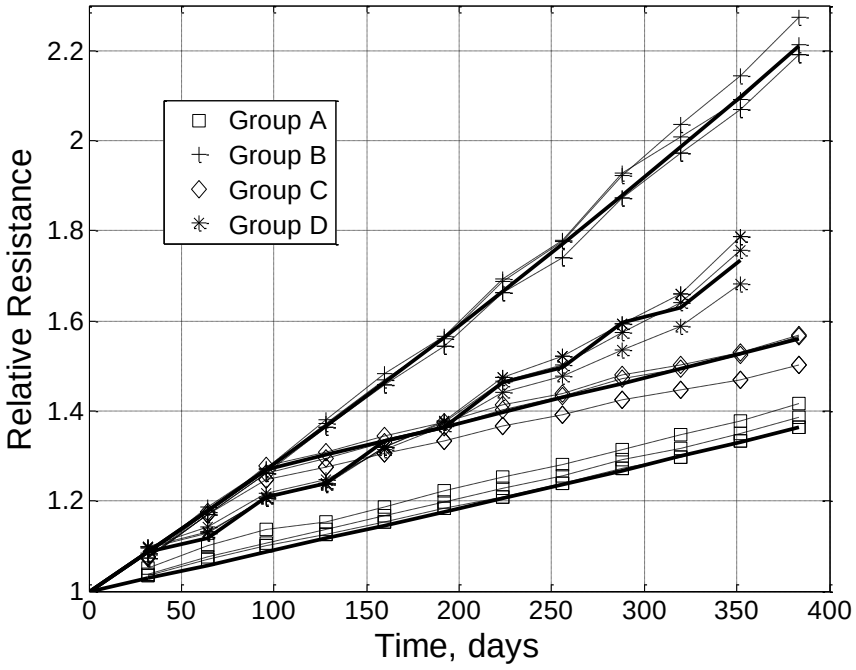

FIGURE 2. Relative resistance vs. time for each group. Data from individual cells are represented by markers that are connected by dashed curves. The fitted model is represented by the heavy, solid curves.

TABLE 4. Estimates of Model Parameters and Variance Components, Relative Resistance

	$\hat{a}$,	$\hat{b}$, °K^{-1}	$\hat{\rho}$	$\hat{\sigma}_\varepsilon^2$	$\hat{\sigma}_\delta^2$
Initial Estimate	-5.35×10^{-2}	1.71×10^{-4}	4.07×10^{-1}	5.0×10^{-5}	1.7×10^{-3}
M.L.	-5.65×10^{-2}	1.80×10^{-4}	3.60×10^{-1}	1.07×10^{-4}	3.0×10^{-3}
Std. Error*	(1.9×10^{-3})	(5.8×10^{-6})	(3.4×10^{-2})	(1.4×10^{-5})	(1.4×10^{-3})

*Std. Error = standard deviation of bootstrap estimates (M.L.)

4.1.1 Assessment of Maximum Likelihood Estimator

The process for obtaining the M.L. estimate ($\widehat{\boldsymbol{\theta}}$) is influenced by the accuracy of the approximations used for the various elements of $\widehat{\boldsymbol{\Sigma}}_j(\boldsymbol{\theta})$ that are used during the numerical optimization process. Based on Equations (12) - (15), these approximations are given in terms of the model parameters. A small simulation study was performed in order to assess the accuracy of these approximations. In this study, various values of $m_j(t)$ were assumed along with the M.L. estimates of σ_ε^2 and σ_δ^2. Assuming normality of δ_j, $\varepsilon_j(0)$, and $\varepsilon_j(t)$, one million values of $M_j(t)$ were simulated via Equation (6) for each value of $m_j(t)$. Figure 3 displays the approximation for $Var\left(M_j(t)\right)$ based on Equation (12) along with the simulated variance of $M_j(t)$ observed for each value of $m_j(t)$. Equation (14) was also found to provide accurate approximations for $Cov\left(M_j(t),\ M_j(t');\ t' \neq t\ \right)$ over the conditions considered. Finally, the distributions of simulated values of $M_j(t)$ were well represented by normal approximations, thus supporting the estimation process that was used.

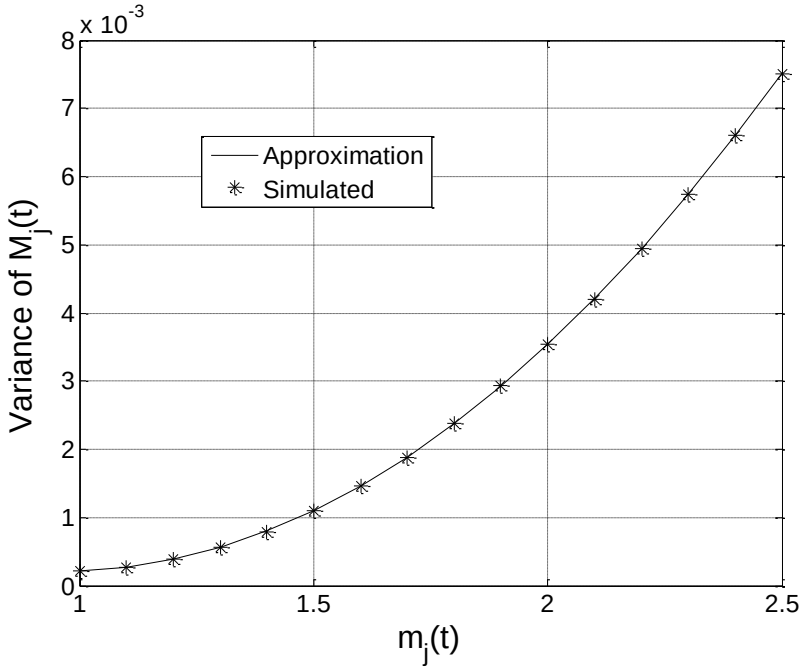

FIGURE 3. Variance (approximated and simulated) of $M_j(t)$ versus $m_j(t)$.

The results from the bootstrap simulation were also used to assess the performance of $\widehat{\boldsymbol{\theta}}$ with respect to each model parameter. Table 5 provides the mean and standard deviation of the 1,000 bootstrap estimates for each of the model parameters. Based on the results in Table 5, we conclude that the M.L. estimator (with the exception of $\hat{\sigma}_\delta^2$) is effectively unbiased for the conditions simulated here. Due to the relatively small sample of cells observed in the experiment (twelve), $\hat{\sigma}_\delta^2$ is an estimate with poor precision and under estimates σ_δ^2 by about 10% on average, which is consistent with the factor $\frac{1}{n_{cells}} = \frac{1}{12}$. Figure 4 displays the distribution of the values of $\hat{\sigma}_\delta^2$ obtained from the bootstrap. Finally note that $\hat{a}$ and $\hat{b}$ are very highly correlated (negatively), with each being only moderately correlated with $\hat{\rho}$. Estimates of the variance components show little correlation with $\hat{a}, \hat{b}$, or $\hat{\rho}$.

TABLE 5. Summary of parameter estimates from bootstrap, relative resistance

	$\hat{a}$,	$\hat{b}$, °K^{-1}	$\hat{\rho}$	$\hat{\sigma}_\varepsilon^2$	$\hat{\sigma}_\delta^2$
Assumed Truth	-5.65×10^{-2}	1.80×10^{-4}	3.60×10^{-1}	1.07×10^{-4}	3.0×10^{-3}
Mean	-5.65×10^{-2}	1.80×10^{-4}	3.61×10^{-1}	1.06×10^{-4}	2.7×10^{-3}
Standard Deviation	1.9×10^{-3}	5.8×10^{-6}	3.4×10^{-2}	1.4×10^{-5}	1.4×10^{-3}

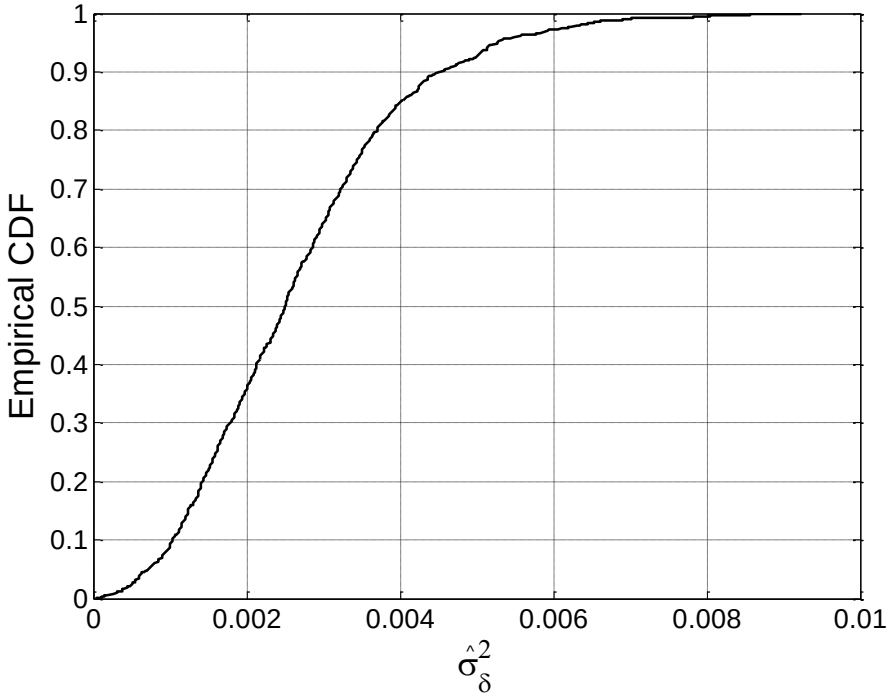

FIGURE 4. Empirical cumulative distribution function of $\hat{\sigma}_\delta^2$ from bootstrap simulations.

4.1.2 Lack of Fit

Since our main interest relates to expected levels of degradation, our primary focus is the fitted degradation model. Lack of fit with respect to the fitted degradation model was measured by using the statistic, $SS_{LOF} = \sum_{i=1}^{4} \sum_{r=1}^{N_{RPT(i)}} \frac{(\bar{M}_{ir} - \hat{m}_{ir})^2}{\hat{\sigma}_{ir}^2 / n_{ir}}$, where the outer sum is indexed by the temperature profile groups and the inner sum is indexed by the reference performance test sequence subsequent to the initial RPT. In all but one case (Group D), $N_{RPT(i)} = 12$. $\bar{M}_{ir}$ (and $\hat{m}_{ir}$) represent the average observed (and predicted) relative performance measure associated with the cells associated with the i^{th} group at the r^{th} RPT. In addition, $\hat{\sigma}_{ir}^2 / n_{ir}$ represents the estimated variance of $\bar{M}_{ir}$ (based on the observational model), where $n_{ir} = 3$ is the number of cells in each treatment group and $\hat{\sigma}_{ir}^2 = (1 + \hat{m}_{ir}(t)^2) \cdot \hat{\sigma}_{\varepsilon}^2 + (\hat{m}_{ir}(t) - 1)^2 \cdot \hat{\sigma}_{\delta}^2$ is the estimated variance of $M_j(t)$ for cells in the i^{th} group at the r^{th} RPT based on Equation (12). The value of SS_{LOF} for the fitted degradation model (69.1) can be compared with the distribution of the values of the lack-of-fit statistics obtained via the bootstrap procedure that is summarized in Fig. 5. Given that the lack-of-fit measure associated with the fitted model is exceeded by about 10% of the bootstrap-generated values, we conclude that there is some (but not overwhelming) statistical evidence for lack of fit. About one-quarter of the SS_{LOF} is associated with two (of the 47) subsets of data (Group A at RPT2 and Group A at RPT3) and three-fourths of the SS_{LOF} is associated with Group A data.

We are also interested in lack of fit as it relates to the estimated variance components. Hence, we would like to assess how well the modeled variance of $M_j(t)$, estimated by $\hat{\sigma}_{ir}^2$, relates to the various values of $\hat{V}ar(M_{ir})$, which denote the sample variances of $M_j(t)$, that are observed within each treatment group / RPT. Figures 6a and 6b enable this comparison by displaying $\hat{\sigma}_{ir}$ and $\sqrt{\hat{V}ar(M_{ir})}$ for each treatment group / RPT versus the predicted relative resistance, $\hat{m}_{ir}(t)$. In Figure 6a, the values of $\hat{m}_{ir}(t)$ and $\hat{\sigma}_{ir}$ were based on the M.L. estimates presented in Table 4. In Figure 6b, the values of $\hat{m}_{ir}(t)$ and $\hat{\sigma}_{ir}$ were based on the initial estimates presented in Table 4. By comparing Figures 6a and 6b it is apparent that $\hat{\sigma}_{ir}$ based on the initial estimates of the variance components reproduced $\sqrt{\hat{V}ar(M_{ir})}$ more closely than estimates of σ_{ir} based on the M.L. estimates of the variance components. This is not surprising given that $\hat{\sigma}_{\delta}^2(init)$ in Equation (18) is largely based on the values of $\hat{V}ar(M_{ir})$ and that

$\hat{\sigma}_{\varepsilon}^2(init)$ in Equation (16) is designed such that $\hat{\sigma}_{ir}^2 \approx \hat{V}ar(M_{ir})$ when $\hat{m}_{ir}(t) \approx 1$. In addition, as previously noted, the M.L. estimate of σ_{δ}^2 has relatively poor precision. Furthermore, a close examination of the results from the bootstrap realizations (based on the fitted degradation and variance component models) reveals that relationships between $\sqrt{\hat{V}ar(M_{ir})}$ and $\hat{\sigma}_{ir}$ (M.L.) such as observed in Figure 6a are not unusual. While the comparison between Figures 6a and 6b suggests that the initial estimates of the variance components might be more credible than the M.L. estimates of the variance components, it is important to re-emphasize that our main interest is associated with the degradation model and its associated parameters (a, b, and ρ). From Table 4, it is clear that the initial and M.L. estimates of the degradation model parameters are very consistent.

At this point we have evaluated the degradation model and the diagonal elements of $\widehat{\boldsymbol{\Sigma}}_j(\boldsymbol{\theta})$ for lack of fit. Other aspects of the fitted degradation and observational models can also be evaluated for lack of fit. For example, consider that the measurements associated with Group D cells were disproportionately small contributors to the log-likelihood function, $\hat{l}(\boldsymbol{\theta}) = \sum_{j=1}^{12} ln\left(f\left(\widehat{\boldsymbol{d}}_{\boldsymbol{j}}; \mathbf{0}, \widehat{\boldsymbol{\Sigma}}_j(\boldsymbol{\theta})\right)\right)$. On average and across RPTs, the Group D measurements seem to straddle the model predictions (see Figure 2). However, a closer examination reveals that, as a group, the Group D measurements are sometimes all above (at RPT1, RPT2, and RPT6) or all below (at RPT5 and RPT9) the model predictions. As a consequence, the observed correlation between certain elements of $\widehat{\boldsymbol{d}}_{\boldsymbol{j}} = \{\hat{d}_{jr} = M_j(r) - \hat{m}_j(r), r = 1{:}\, n_r\}$ is strongly negative for Group D cells (e.g., between $\hat{d}_{j1}$ and $\hat{d}_{j5}$). This behavior is hard to reconcile with the expected positive correlation between the elements of $\widehat{\boldsymbol{d}}_{\boldsymbol{j}}$ that is described by Equation (14) and is likely a source of Group D's meager contribution to the log-likelihood function. Perhaps this is indicative of a temperature control issue given that Group D cells experienced frequent changes in stress.

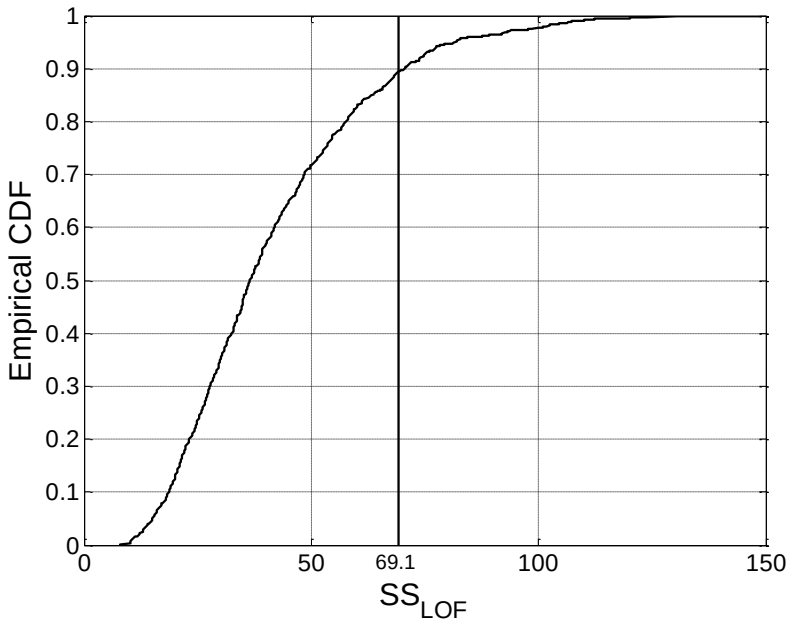

FIGURE 5. Empirical cumulative distribution function of SS_{LOF} from bootstrap simulations compared with the value of SS_{LOF} (69.1) based on the fitted relative resistance model.

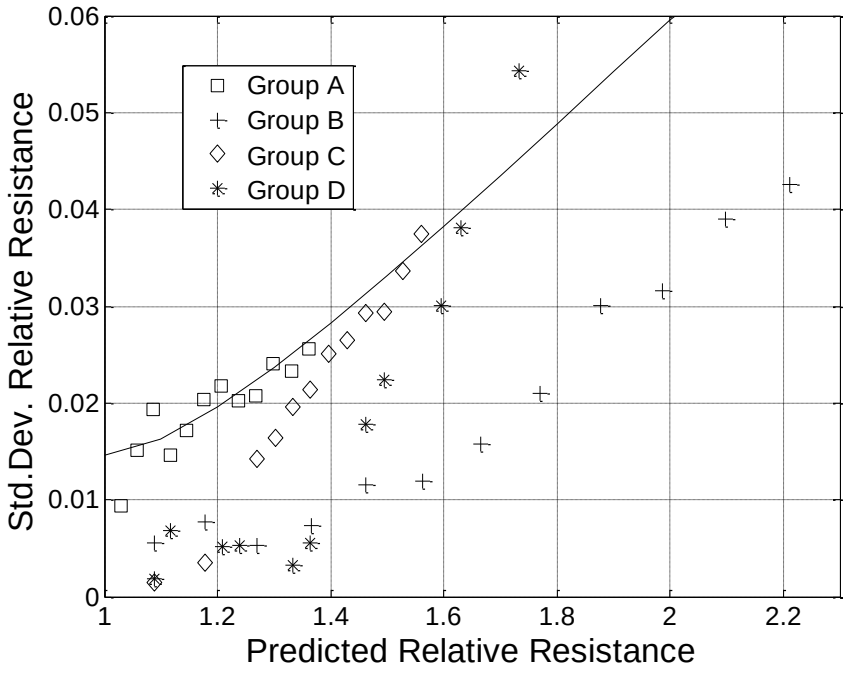

FIGURE 6a. Standard deviation of relative resistance within each treatment group/RPT (markers) compared with $\hat{\sigma}_{ir}$ (solid curve) versus $\hat{m}_{ir}(t)$ using ML parameter estimates.

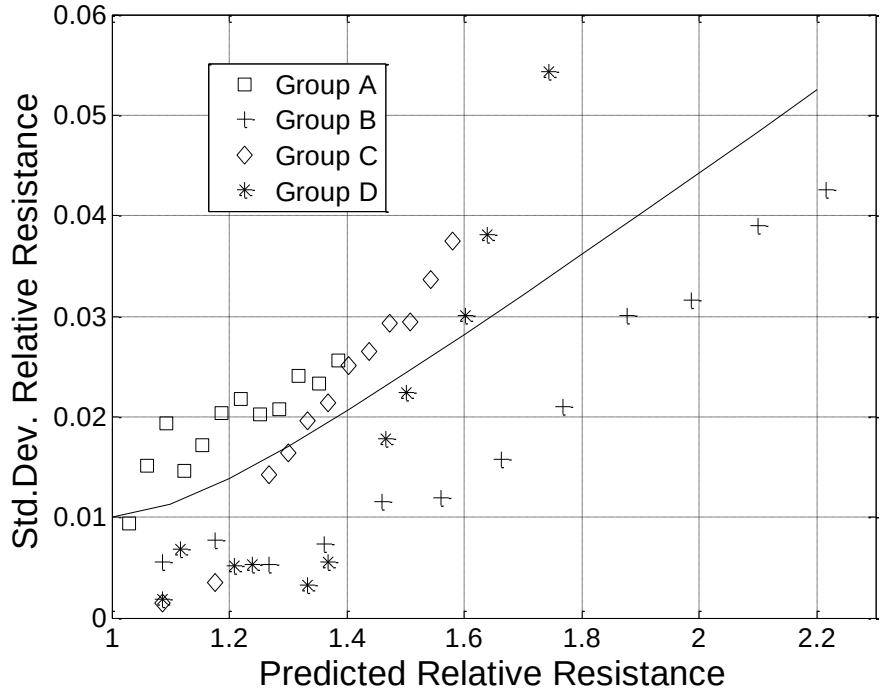

FIGURE 6b. Standard deviation of relative resistance within each treatment group/RPT (markers) compared with $\hat{\sigma}_{ir}$ (solid curve) versus $\hat{m}_{ir}(t)$ using initial parameter estimates.

4.1.3 Comparison with Reduced Model

For purposes of comparison, it is interesting to consider a reduced form of the full degradation model described in Equation (1). That is, consider

$$\frac{dm(T[0,\tau])}{d\tau} = k(T(\tau)), \tag{20}$$

where $k\big(T(\tau)\big) = a + b \cdot T(\tau)$. Note that the model given in Equation (1) reduces to the model given in Equation (20) when $\rho = 0$. Thus, one can examine the evidence for the full model versus the reduced model by testing whether or not ρ is distinguishable from zero. In the reduced model, the degradation rate remains constant over time for a given temperature and as such is consistent with existing rate-based modelling approaches (e.g., see Tseng and Wen 2000, Chan and Meeker 2001, and Peng and Tseng 2010) where the degradation rate depends only on the current stress and not on the current state of the degradation measure. By assuming the same observational model as described in Equations 4-6, Figure 7 illustrates the fit of the reduced model to the experimental data that is achieved by using the methods described in Section 3.3.

In this case, the M.L. estimates of the degradation and observational model parameters are $\hat{a} = 6.34 \times 10^{-2}$, $\hat{b} = 2.02 \times 10^{-4}$, $\hat{\sigma}_{\varepsilon}^2 = 1.89 \times 10^{-4}$ and $\hat{\sigma}_{\delta}^2 = 5.4 \times 10^{-3}$. The most remarkable difference between the model fits represented in Figures 2 and 7 is with regard to the Group B data. It is clear that the additional parameter associated with the full model (ρ) is helpful to represent the increasing rate of resistance increase that is exhibited most strongly by the Group B cells. This supports the utility of $\hat{\rho}$ in the fitted full model, where ρ was found to be distinguishable from zero. Also, the estimated variance components associated with the reduced model are noticeably larger, presumably due to lack of fit.

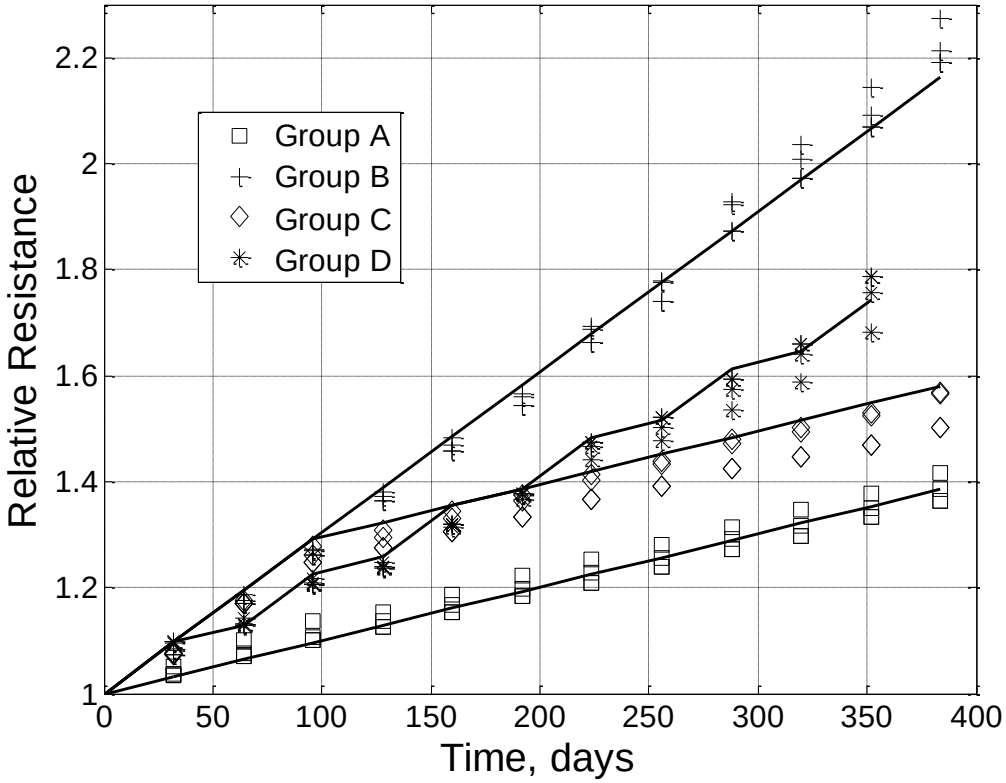

FIGURE 7. Relative resistance vs. time for each group, reduced model. The data are represented by the markers, and the curves are the results of fitting the reduced model.

4.2 **Capacity**

Figures 8a and 8b illustrate how the fitted inverse relative capacity model obtained by M.L. estimation relates to the experimental data (by group) for all profiles. The initial and M.L. estimates of the degradation model parameters (a, b, and ρ) and variance components (σ_{ε}^2 and

σ_δ^2) are given in Table 6. Note that the initial and M.L. estimates of the degradation model parameters are similar. Unlike in the case of relative resistance (where $\hat{\rho}$ was positive), $\hat{\rho}$ is negative. This is consistent with the divergence in behavior between relative resistance and inverse relative capacity that begins at about 1.6 relative units as shown in Figure 1. Given that the average initial capacity was about 1.26 Ah, it follows that the standard deviation of measurement error is estimated by M.L. to be about 0.009 Ah and the rate of relative capacity decrease across cells varies with an estimated standard deviation of about 3%. It is interesting to note that 0.009 Ah is equal to the entire range of capacity observed across the initial measurements (see Table 3), suggesting that M.L. is overestimating σ_ε^2. The initial estimate of σ_ε^2 seems more credible and leads to an estimated standard deviation of measurement error of about 0.004 Ah. The value of SS_{LOF} for the fitted degradation model (242) can be compared with the distribution of the lack-of-fit statistics obtained via the bootstrap procedure that is summarized in Fig. 9. Clearly, we can conclude that there is significant statistical evidence for overall lack of fit as the SS_{LOF} associated with the fitted model is far off scale. The lack of fit, which can easily be visualized in Figs. 8a and 8b, is associated with all groups at RPT1 and Group D at all RPT's. Also, the fitted model does not capture the behavior of Group B cells at the later RPT's where it seems that the degradation rate is slowing more than predicted.

TABLE 6. Estimates of model parameters and variance components, inverse relative capacity

	$\hat{a}$,	$\hat{b}$, °K^{-1}	$\hat{\rho}$	$\hat{\sigma}_\varepsilon^2$	$\hat{\sigma}_\delta^2$
Initial Estimate	-5.75×10^{-2}	1.84×10^{-4}	-2.44×10^{-1}	8.0×10^{-6}	8.0×10^{-4}
M.L.	-5.81×10^{-2}	1.86×10^{-4}	-2.85×10^{-1}	5.43×10^{-5}	1.17×10^{-3}
Std. Error*	(1.9×10^{-3})	(6.1×10^{-6})	(6.0×10^{-2})	(6.4×10^{-6})	(6.2×10^{-4})

*Std. Error = standard deviation of bootstrap estimates (M.L.)

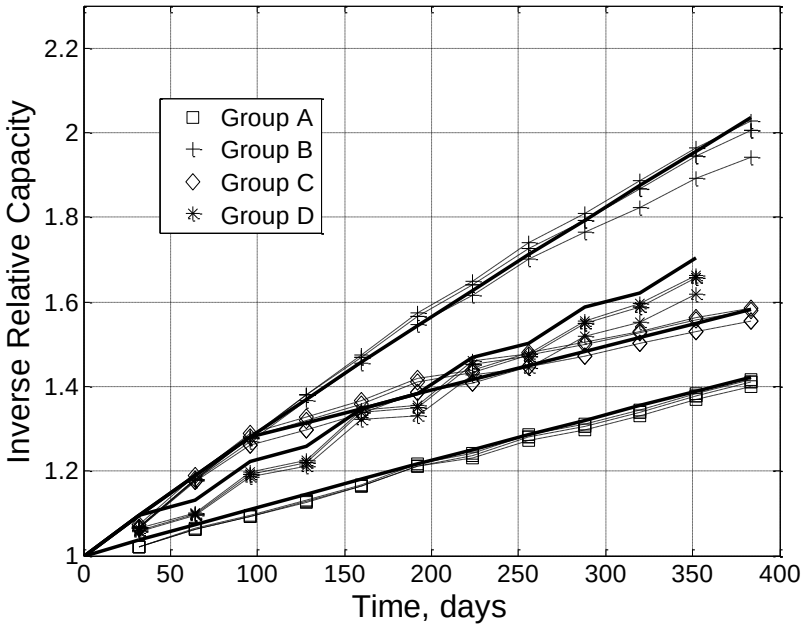

FIGURE 8a. Inverse relative capacity vs. time for all groups. Data from individual cells are represented by markers that are connected by dashed curves. The fitted model is represented by the heavy, solid curves.

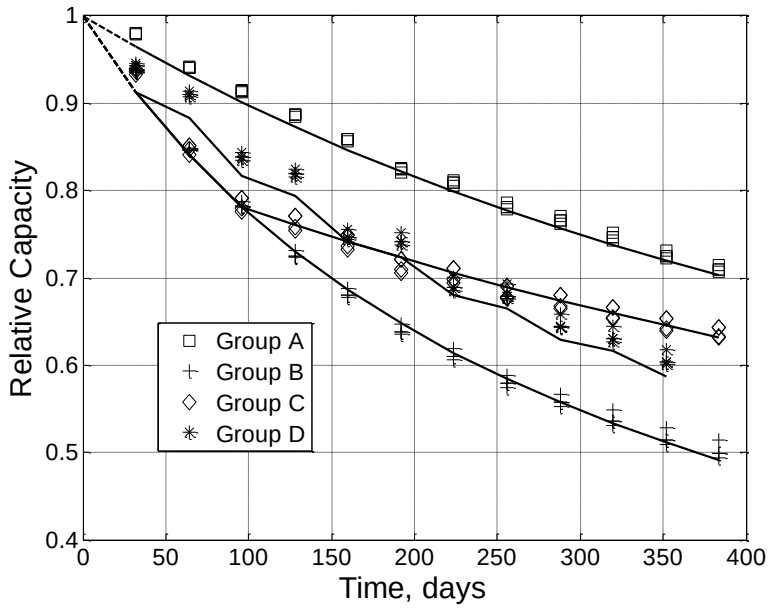

FIGURE 8b. Relative capacity vs. time for all groups. Data from individual cells are represented by markers. The fitted model is represented by the curves.

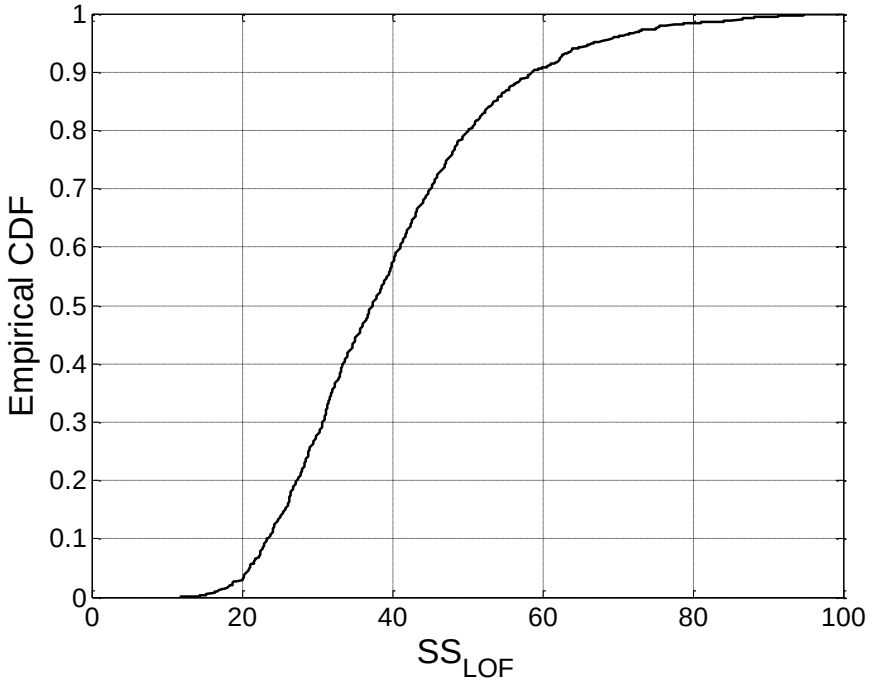

Fig. 9. Empirical cumulative distribution function of SS_{LOF} from bootstrap simulations, inverse relative capacity model.

Without understanding the actual source(s) of the lack of fit that is observed with respect to the degradation model, it is clear that the model is inaccurate for predicting capacity during the early part of the degradation process. The actual capacity lost between RPT0 and RPT1 is less than predicted for all stress conditions. However, the model seems to predict levels of cumulative degradation reasonably well after RPT1 for all stress conditions except in the case of Group D cells.

The fitted degradation models for relative resistance and relative inverse capacity are similar yet distinct. Measured by $\hat{b}$, the estimated effect of temperature on the rate expression, $k\big(T(\tau)\big)$, is similar for the two measures. However, whereas the rate of increase in resistance seems to increase over time (positive value of $\hat{\rho}$), the rate of increase in inverse capacity seems to decrease over time (negative value of $\hat{\rho}$). Clearly, ρ is useful to differentiate the subtle difference in the aging behavior of resistance and inverse capacity. Nevertheless, the similarity of these models is perhaps indicative of substantial commonality between the temperature-related mechanisms that cause the increase of resistance and the decrease in capacity. The degradation behavior of

capacity seems to be more complex than that of resistance, primarily due to the smaller than expected level of capacity decrease observed between RPT0 and RPT1. Finally, the discordant behavior of Group D cells is not well understood. We speculate that this might have been caused by a temperature control issue, although we have no firm evidence of such.

5. Discussion and Conclusions

Here, we are concerned with whether or not a degradation processes can be considered to be memoryless, meaning the degradation rate depends only on the current state and current stress level. If the future degradation from the current state depends on how the process arrived at the current state, then we would conclude that the degradation process has memory and that the degradation measure considered is not a complete indicator of state. Furthermore, it is unlikely that such a measure could provide useful predictions of degradation in non-constant stress environments.

In the case study presented here, the aging behavior of a particular design of lithium-ion cells was studied under isothermal and non-isothermal calendar aging conditions in the temperature range of 45 to 55°C. Simple rate-based empirical models were developed and used to predict resistance increase and capacity decrease over both isothermal and non-isothermal conditions. Resistance increase appears to be reasonably well approximated by a memoryless process over the conditions studied for this particular cell chemistry/design based on the closeness of the fitted relative resistance model to the resistance data. The decrease in capacity was found to be somewhat more complex. Significant lack of fit was observed in certain instances, particularly early on in the degradation process. The implication is that relative resistance after exposure to a temperature profile within the range of conditions considered, can be well approximated by Equation (2). Furthermore, if this behavior extrapolates to use conditions, one could use these models to accurately predict the resistance rise in complex thermal environments such as found in automotive battery applications. Confirmation of these observations using additional experimentation involving realistic temperature paths at lower temperatures would be required in order to validate this conjecture.

The form of the proposed rate-based degradation model, which is inherently memoryless, assumes a non-decreasing relative response and has the flexibility to portray an overall degradation rate (across stress levels) that is either increasing, decreasing, or remaining steady

over time. The advantage of the proposed rate-based model over existing rate-based models, which assume a constant degradation rate at a given stress level, was clearly demonstrated in the example. We believe that broadening the degradation rate dependence to include the current degradation state could be useful in other contexts involving non-constant or constant stress. Although we specified a particular form for the degradation rate in the example, other forms are possible and would need to be appropriate for the situation of interest. Our particular observational model reflects the apparent random unit-to-unit variability in the degradation rate that is perceived in our example. In other situations, the variability in degradation paths within a treatment group might be better represented by some other model, perhaps Brownian motion.

Finally, a three-step process was used to estimate the parameters associated with the expected degradation rate and the magnitude of the variance components associated cell-to-cell variation and measurement error. The final step involved joint maximum likelihood estimation of the three degradation rate parameters and both variance components. Parametric bootstrap simulations were used to estimate parameter uncertainties as well as assess the performance of the maximum likelihood estimator. In the context considered, we assess the maximum likelihood estimator to be effectively unbiased for all dimensions except for the variance component associated with cell-to-cell variation in the degradation rate. This variance component tends to be under estimated due to the small number of cells studied.

Acknowledgments

We thank the editor and referees for comments that have led to an improved paper. The authors at Argonne gratefully acknowledge support from the U. S. Department of Energy (DOE), Office of Energy Efficiency and Renewable Energy, Vehicle Technologies Office. Argonne National Laboratory is operated for DOE Office of Science by UChicago Argonne, LLC, under contract number DE-AC02-06CH11357. The efforts at Idaho National Laboratory and at Lawrence Berkeley National Laboratory were performed under Contract Numbers DE-AC07-05ID14517 and DE-AC03-76SF00098, respectively.

References

Anseán, D., González, M., Viera, J. C., García, V. M., Blanco, C., and Valledor, M. (2013). "Fast Charging Technique for High Power Lithium Iron Phosphate Batteries: A Cycle Life Analysis". *Journal of Power Sources*, 239, pp. 9-15.

Barré, A., Deguilhem, B., Grolleau, S., Gérard, M., Suard, F., and Riu, D. (2013). "A Review on Lithium-ion Battery Ageing Mechanisms and Estimations for Automotive Applications". *Journal of Power Sources*, 241, pp. 680-689.

Battery Calendar Life Estimator Manual, Modeling and Simulation, Rev. 1 (2012). INL-EXT-08-15136, Idaho National Laboratory, Idaho Falls, ID.

Battery Test Manual for Plug-In Hybrid Electric Vehicles, Rev. 3 (2014). INL/EXT-14-32849, Idaho National Laboratory, Idaho Falls, ID.

Bloom, I., Jones, S. A., Battaglia, V. S., Henriksen, G. L., Christophersen, J. P., Wright, R. B., Ho, C. D., Belt, J. R., and Motloch, C. G. (2003). "Effect of Cathode Composition on Capacity Fade, Impedance Rise and Power Fade in High-power, Lithium-ion Cells". *Journal of Power Sources*, 124, pp. 538-550.

Broussely, M., Biensan, Ph., Bonhomme, F., Blanchard, Ph., Herreyre, S., Nechev, K., and Staniewicz, R. J. (2005). "Main aging mechanisms in Li ion batteries". *Journal of Power Sources*, 146, pp. 90-96.

Cai, M., Yang, D., Tian, K., Chen, W., Chen, X., Zhang, P., Fan, X., and Zhang, G. (2016). "A Hybrid Prediction Method on Luminous Flux Maintenance of High-power LED Lamps". *Applied Thermal Engineering*, 95, 482-490.

Chan, V. and Meeker, W. Q. (2001). "Estimation of Degradation-based Reliability in Outdoor Environments". Technical Report, Department of Statistics, Iowa State University.

Christophersen, J. P., Bloom, I., Thomas, E. V., Gering, K. L., Henriksen, G. L., Battaglia, V. S., & Howell, D. (2006). *Advanced Technology Development Program for Lithium-ion Batteries: Gen 2 Performance Evaluation Final Report* (No. INL/EXT-05-00913). Idaho National Laboratory (INL).

Christophersen, J. P., Hunt, G. L., Ho, C. D., & Howell, D. (2007). “Pulse Resistance Effects due to Charging or Discharging of High-power Lithium-ion Cells: A Path Dependence Study”. *Journal of Power Sources*, 173, pp. 998-1005.

Efron, B. and Tibshirani, R. J. (1993). *An Introduction to the Bootstrap*, Chapman and Hall, London, UK.

Escobar, L. A. and Meeker, W. Q. (2006). “A review of accelerated test models”. *Statistical Science*, pp. 552-577.

Gering, K. L., Sazhin, S. V., Jamison, D. K., Michelbacher, C. J., Liaw, B. Y., Dubarry, M., & Cugnet, M. (2011). “Investigation of Path Dependence in Commercial Lithium-ion Cells Chosen for Plug-in Hybrid Vehicle Duty Cycle Protocols”. *Journal of Power Sources*, 196, pp. 3395-3403.

Han, X., Ouyang, M., Lu, L., Li, J., Zheng, Y., and Li, Z. (2014). “A Comparative Study of Commercial Lithium Ion Battery Cycle Life in Electrical Vehicle: Aging Mechanism Identification”. *Journal of Power Sources*, 251, pp. 38-54.

Holland, P. W. and Welsch R. E. (1977). "Robust Regression using Iteratively Reweighted Least-Squares”. *Communications in Statistics-Theory and Methods*, 6, pp. 813-827.

Lagarias, J.C., Reeds, J. A., Wright, M. H., and Wright, P. E. (1998), "Convergence Properties of the Nelder-Mead Simplex Method in Low Dimensions," *SIAM Journal of Optimization*, 9, pp. 112-147.

Liu, T., Cheng, L., Pan, Z., and Sun, Q. (2016). “Cycle Life Prediction of Lithium-ion Cells Under Complex Temperature Profiles”. *Eksploatacja i Niezawodnosc – Maintenance and Reliability*, 18, pp. 25-31.

Meeker, W. Q. and Escobar, L. A. (1998). *Statistical Methods for Reliability Data*, John Wiley, New York, NY.

Meeker, W. Q., Escobar, L. A., and Lu, C. J. (1998). “Accelerated Degradation Tests: Modeling and Analysis”. *Technometrics*, 40, pp. 89-99.

Nelson, W. B. (2004). *Accelerated Testing, Statistical Models, Test Plans and Data Analysis*, John Wiley, Hoboken, NJ.

Park, J. I. and Bae, S. J. (2010). “Direct Prediction Methods on Lifetime Distribution of organic light-emitting diodes from accelerated degradation tests”. *IEEE Transactions on Reliability* 59, pp. 74-90.

Peng, C. Y. and Tseng, S. T. (2010). “Progressive-stress Accelerated Degradation Test for Highly-reliable Products”. *IEEE Transactions on Reliability*, 59, pp. 30-37.

Santini, T., Morand, S., Fouladirad, M., Phung, L. V., Miller, F., Foucher, B., Grall, A., and Allard, B. (2014). “Accelerated Degradation Data of SiC MOSFETs for Lifetime and Remaining Useful Life Assessment”. *Microelectronics Reliability*, 54, pp. 1718-1723.

Thomas, E. V., Bloom, I., Christophersen, J. P., and Battaglia, V. S. (2008). “Statistical Methodology for Predicting the Life of Lithium-ion Cells via Accelerated Degradation Testing”. *Journal of Power Sources*, 184, pp. 312-317.

Thomas, E. V., Bloom, I., Christophersen, J. P., and Battaglia, V. S. (2012). “Rate-based Degradation Modeling of Lithium-ion Cells”. *Journal of Power Sources*, 206, pp. 378-382.

Tseng, S. T. and Wen, Z. C. (2000). “Step-stress Accelerated Degradation Analysis for Highly Reliable Products. *Journal of Quality Technology*, 32, pp. 209-216.

Vetter, J., Novák, P., Wagner, M. R., Veit C., Möller, K.-C., Bensenhard, J. O., Winter, M., Wohlfahrt-Mehrens, M., Vogler, C., and Hammouche, A. (2005). “Ageing Mechanisms in Lithium-ion Batteries”. *Journal of Power Sources*, 147, pp. 269-281.

Wang, Y. H. and Wong, D. S. H. (2015). “Modelling Accelerated Degradation Test and Shelf-life Prediction of Dye-sensitized Solar Cells with Different Types of Solvents”. *Solar Energy*, 118, pp. 600-610.

Wohlfahrt-Mehrens, M., Vogler, C., and Garche, J. (2004). “Aging Mechanisms of Lithium Cathode Materials”. *Journal of power sources*, 127, pp. 58-64.

Wright, R. B., Motloch, C. G., Belt, J. R., Christophersen, J. P., Ho, C. D., Richardson, R. A., Bloom, I., Jones, S. A., Battaglia, V. S., Henriksen, T, Unkelhaeuser, T., Ingersoll, D., Case, H. L., Rogers, S. A., and Sutula, R. A. (2002). “Calendar-and Cycle-life Studies of Advanced Technology Development Program Generation 1 Lithium-ion Batteries”. *Journal of Power Sources*, 110, pp. 445-470.

Xia, J., Nie, M., Ma, L., and Dahn, J. R. (2016). “Variation of Coulombic Efficiency Versus Upper Cutoff Potential of Li-ion cells Tested with Aggressive Protocols”. *Journal of Power Sources*, 306, pp. 233-240.

Yang, Z., Chen, Y. X., Li, Y. F., Zio, E., & Kang, R. (2014). “Smart Electricity Meter Reliability Prediction Based on Accelerated Degradation Testing and Modeling”. *International Journal of Electrical Power & Energy Systems*, 56, pp. 209-219.

Zhang, S. S. (2006). “The Effect of the Charging Protocol on the Cycle Life of a Li-ion Battery”. *Journal of Power Sources*, 161, pp. 1385-1391.